DRAFT: LARGE-EDDY SIMULATION AND CONJUGATE HEAT TRANSFER AROUND A LOW-MACH TURBINE BLADE

Florent Duchaine[*]
CERFACS
42 avenue G. Coriolis
31 057 Toulouse Cedex 01
France
Email: florent.duchaine@cerfacs.fr

Nicolas Maheu
Vincent Moureau
CORIA
CNRS UMR6614 Universitée et INSA de Rouen
Saint-Etienne du Rouvray
France
Email: nicolas.maheu@coria.fr
Email: vincent.moureau@coria.fr

Guillaume Balarac
LEGI
CNRS UMR5519
Université Joseph Fourier
et Institut National Polytechnique de Grenoble
Grenoble
France
Email: guillaume.balarac@grenoble-inp.fr

Stéphane Moreau
Mechanical Engineering
Université de Sherbrooke
2500 blvd de lUniversité
Sherbrooke QC J1K2R1
Canada
Email: stephane.smoreau@gmail.com

ABSTRACT

Determination of heat loads is a key issue in the design of gas turbines. In order to optimize the cooling, an exact knowledge of the heat flux and temperature distributions on the airfoils surface is necessary. Heat transfer is influenced by various factors, like pressure distribution, wakes, surface curvature, secondary flow effects, surface roughness, free stream turbulence and separation. All these phenomenon are challenges for numerical simulations. Among numerical methods, Large Eddy Simulations (LES) offers new design paths to diminish development costs of turbines through important reductions of the number of experimental tests. In this study, LES is coupled with a thermal solver in order to investigate the flow field and heat transfer around a highly loaded low pressure water-cooled turbine vane at moderate Reynolds number (150 000). The meshing strategy (hybrid grid with layers of prisms at the wall and tetrahedra elsewhere) combined with a high fidelity LES solver gives accurate predictions of the wall heat transfer coefficient for isothermal computations. Mesh convergence underlines the known result that wall-resolved LES requires discretisations for which y^+ is of the order of one. The analysis of the flow field gives a comprehensive view of the main flow features responsible of heat transfer, mainly the separation bubble on the suction side that triggers transition to a turbulent boundary layer and the massive separation region on the pressure side. Conjugate heat transfer computation gives access to the temperature distribution in the blade, which is in good agreement with experimental measurements. Finally, given the uncertainty on the coolant water temperature provided by experimentalist, uncertainty quantification allows apprehending the effect of this parameter on the temperature distribution.

NOMENCLATURE
A   SYMBOLS
C Blade chord
C_s Solid heat capacity
c_p Fluid heat capacity at constant pressure
E Total Energy
e_s Sensible energy
h Heat transfer coefficient
P Pressure

---

[*]Address all correspondence to this author.

1

P_1^t Total inlet pressure
Pr_t Turbulent Prandtl number
q Heat flux
q_{wall} Wall heat flux
r Mixture gas constant
s Curvilinear abscissa
T Temperature
T_1^t Total inlet temperature
T_{wall} Wall temperature
$\overline{T}_{CHT}$ Mean value of the conjugate heat transfer temperature profile
u Velocity
x^+, y^+, z^+ Dimensionless wall distances
ρ Fluid density
ρ_s Solid density
λ_s Solid heat conductivity
λ_t Sub-grid scale turbulent heat conductivity
ν_t Sub-grid scale turbulent viscosity
$\Delta x, \Delta y, \Delta z$ Discretisation sizes
τ_w Wall friction
τ_f Fluid characteristic time
τ_s Solid characteristic time
$\sigma_{\overline{T}_{CHT}}$ Standard deviation of the conjugate heat transfer temperature profile

B   ACRONYMS

CFD   Computational Fluid Dynamics
CFL   CourantFriedrichsLewy number
CHT   Conjugate Heat Transfer
DNS   Direct Numerical Simulation
FTT   Flow Through Time
HTC   Heat Transfer Coefficient
LES   Large Eddy Simulation
RANS   Reynolds Averaged Navier-Stokes
SGS   Sub-Grid Scale
UQ   Uncertainty Quantification

INTRODUCTION

Determination of heat loads such as wall temperatures and heat fluxes, is a key issue in gas turbine design [1–5]: the interaction of hot gases with colder walls is an important phenomenon and a main design constraint for turbine blades. In recent gas turbines, the constant increase of the thermodynamic efficiency leads to turbine inlet temperature that is far beyond the materials melting point. As a result, optimized cooling technologies are necessary to ensure the life time of the engine without reducing its efficiency. An exact knowledge of the heat transfer distribution on the airfoils surface is thus necessary. Heat transfer around vanes is influenced by various factors, as pressure distribution, wakes, surface curvature, secondary flow effects, surface roughness, free stream turbulence and separation. Low pressure blades

of gas turbine are a typical example of configuration where separations can occur on both pressure and suction sides of the airfoil because of different flow features.

With the constant increase of computing power, numerical simulations of the thermal interaction between fluid flows and solids offer new design paths to diminish development costs through important reductions of the number of experimental tests. When a Computational Fluid Dynamics (CFD) solver is coupled to a heat transfer solver, the accuracy of the coupled tool is generally controlled by the fluid code. To resolve the fluid flow, a large range of numerical methods is nowadays available in the literature, all of which are more or less suited to near wall flows [6–11]. Conventional CFD techniques use Reynolds Averaged Navier-Stokes (RANS) methods that require all the turbulent scales of the flow to be modeled putting stringent modeling effort on the turbulent closures near walls [12–15]. While such approaches are routinely used in the design phase of turbine vanes [16,17], they cannot capture all the complex effects of turbomachinery flows and looking for more precise flow solvers is a usual objective in this field. Fully unsteady numerical methods where all turbulent scales (Direct Numerical Simulations, DNS) or parts of the scales (large Eddy Simulation, LES) are solved for are also available. Although the former is clearly out of reach for real applications, the latter still requires to prove its efficiency. Recent contributions based on LES [11, 18–21] provide promising results especially for the prediction of heat transfer in complex geometries [22–25].

The present study aims at investigating the use of high fidelity LES for the prediction of Conjugate Heat Transfer (CHT) in a highly loaded low pressure water-cooled turbine blade submitted to transitional flows with massively separation. The resolution of the CHT problem rely on the coupling between a flow solver and a conduction code that exchange boundary conditions at their interface [22]. This solution has the advantage of using existing state-of-the-art codes to solve fluid and solid equations [26–31]. Uncertainty quantification of the solid model parametrization is studied in order to gauge the sensitivity of the coupled results to experimental uncertainties.

The low pressure turbine cascade and the associated experiment are first presented. Then the LES fluid and solid solvers are introduced and the numerical setup in is detailed. A grid convergence study is achieved and the flow field as well as heat transfer characteristics obtained by the simulations are discussed and compared with experimental data. Then, thermal results given by the CHT computations are presented and related to the main flow structures that control heat transfer. Finally, the last section proposes to quantify the role of the uncertainty on solid conductivity as well as on convective conditions inside the cooling channels of the blade.
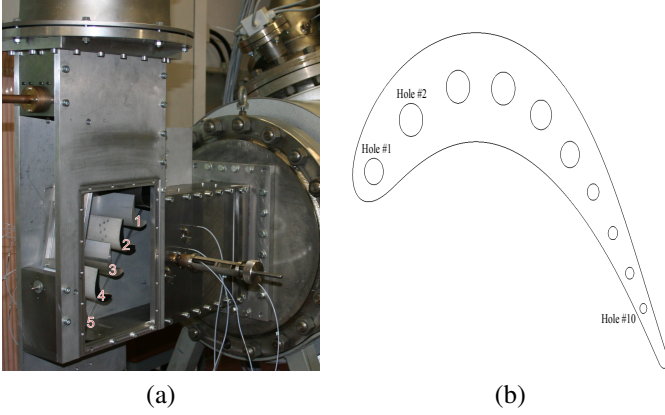
(a)   (b)

FIGURE 1. (a) TEST SECTION - BLADES WITH PRESSURE TAPS #2 AND #4, BLADE WITH THERMOCOUPLES #3, (b) GEOMETRY OF THE COOLED BLADE #3.

EXPERIMENTAL SETUP AND CONDITIONS

The tested configuration is a 2D highly loaded low pressure turbine blade cascade, largely described in [32] and displayed in Fig. 1. This blade was investigated in the European research project *Aero-Thermal Investigation on Turbine End-Wall and Blades* (AITEB-2, 6FP, AST4-CT-2005-516113). The aim of the blade design was to generate an extended recirculation bubble on the pressure side at nominal conditions. The objective of the experimental study was to document flow field and heat transfer of a highly loaded low pressure turbine airfoil with a long separation bubble on the pressure side. For these investigations a linear cascade with a water-cooled airfoil was used.

The cascade consists of five untwisted turbine blades of which the inner three blades are instrumented (Fig. 1-a). Blades 2 and 4 (Fig. 1) are equipped with pressure taps for measuring the pressure distribution. For the heat transfer measurements, blade 3 is water-cooled by 10 cooling channels (Fig. 1-b). Moreover this blade is instrumented with 40 thermocouples for temperature measurements. The airfoils material is a titanium alloy for which experimentalists give a thermal conductivity of about $\lambda_s \approx 7\ \mathrm{W \cdot m^{-1} \cdot K^{-1}}$.

Ladisch *et al.* [32] have determined the distribution of heat transfer coefficients (HTC) along the blade surface $h(s)$ with an iterative process by adjusting a finite-element thermal model in order to fit to the temperature measurements given the inlet total temperature T_1^t and the cooling temperatures [33–35]. The HTC at the position s is thus defined by the ratio between the wall heat flux, $q_{wall}(s)$, and the difference between the total free stream temperature, T_1^t and the local wall temperature $T_{wall}(s)$:

$$h(s) = \frac{q_{wall}(s)}{T_1^t - T_{wall}(s)} \qquad (1)$$

Inlet Mach number		0.068
Oulet Mach number		0.116
Inlet Reynolds number		93 101
Oulet Reynolds number		158 088
Inlet total pressure	P_1^t	102 274.8 *Pa*
Inlet total temperature	T_1^t	348.06 *K*
Outlet static pressure		101315.9 *Pa*

Errors for the heat transfer coefficient were estimated in a range up to 10% for most of the blade surface and up to 15% near the leading and trailing edges, where the distance between the thermocouples and the cooling channels is small.

A set of experiments have been conducted at various free-stream turbulence intensities and Reynolds numbers of the inflow [32]. Exit Reynolds numbers based on the chord C length and the nominal exit velocity ranging from 75000 to 500000 were considered. The turbulence level was varied between 1.6% and 10%. The experimental results reveal a considerable influence of the boundary layer separation on the local heat transfer. The size of the separation region on the pressure side is strongly influenced by free-stream turbulence level and Reynolds number. Moreover, the influence of this separation is clearly visible in the heat transfer distributions: heat transfer on the pressure side is mainly governed by the extent of the separation bubble.

In all experimental conditions the boundary layer on the pressure side separates. An increase of either the Reynolds number or the free-stream turbulence level leads to a shortening of the separation region. On the suction side the laminar boundary layer is affected by turbulent fluctuations in the free stream for high Reynolds numbers. Furthermore, a separation bubble due to a strong adverse pressure gradient occurs on the suction side for low Reynolds numbers and turbulence levels. With increasing both Reynolds number and turbulence level this separation disappeared and a bypass transition takes place. So for high Reynolds numbers there is a strong effect of turbulence on heat transfer on the suction side whereas for low Reynolds number the effect on the pressure side is stronger.

The experimental configuration explored in this study corresponds to the lowest turbulence level (1.6%) and to an exit Reynolds number of 150 000 (Tab. 1). The lowest turbulence level is chosen in order to avoid dealing with turbulence injection issues [25] (injection method, length scale of the eddies, mesh resolution to transport the eddies until the blade ...) and to concentrate on the physics around the blade itself. As a result, the

computations without turbulence injection are considered comparable to experimental results with a turbulent level of 1.6%. The Reynolds number of 150 000 is retained because experimental results at this point exhibits representative comportments of a real low pressure turbine for the treatment of conjugate heat transfer such as a large separation on the pressure side and separation bubble due to adverse pressure gradient on the suction side. While undoubtedly this limited Reynolds number imposes less constraints on the number of grids points to resolve boundary layers than higher Reynolds number, such flow features are challenging to capture accurately with LES [36].

NUMERICAL APPROACH

The method adopted to compute the conjugate heat transfer (CHT) in the blade is to couple a parallel LES solver with a conduction code. Efficient implementation of such a CHT framework requires a software to manage the parallel execution of the solvers as well as the data exchanges during their execution. In order to insure the performance of the coupling, a fully parallel code coupler is used [37,38]. This section describes the fluid and conduction solvers as well as the numerical setup used to model the blade.

Governing equations and LES models.

The initial governing equations solved are the unsteady compressible Navier-Stokes equations that describe the conservation of mass, momentum and energy. For compressible turbulent flows the primary variables are the density ρ, the velocity vector u_i and the total energy $E \equiv e_s + 1/2\, u_i u_i$. The fluid follows the ideal gas law, $p = \rho\, r\, T$ and $e_s = \int_0^T c_p\, dT - p/\rho$, where e_s is the sensible energy, p the pressure, T the temperature, c_p the fluid heat capacity at constant pressure and r is the mixture gas constant. The LES solver takes into account changes of heat capacity with temperature using tabulated values of heat capacities. The viscous stress tensor and the heat diffusion vector use classical gradient approaches. The fluid viscosity follows Sutherland's law and the heat diffusion coefficient follows Fourier's law. The application of the filtering operation to the instantaneous set of compressible Navier-Stokes transport equations yields the LES transport equations [39] which contain Sub-Grid Scale (SGS) quantities that need modelling [11, 40]. The unresolved SGS stress tensor is modelled using the Boussinesq assumption [8, 41, 42]. The σ-model [43, 44], based on the analysis of the singular values of the resolved velocity gradient tensor, is chosen to model the SGS viscosity ν_t. The σ-model was developed to overcome some drawbacks observed on most of the static models without using additional test filter. Indeed, the model presents the interesting property to vanish in various laminar flow configurations for which no SGS activity is expected: (1) it automatically vanishes as soon as the resolved field is two-dimensional (including the pure shear and solid ro-

tation cases); (2) it generates no subgrid-scale dissipation when the resolved scales are in pure axisymmetric or isotropic contraction/expansion (the former situation corresponds to the impact region of a laminar round jet impinging on a solid plate, the latter is representative of an acoustic monopole); (3) it has the appropriate cubic behavior in the vicinity of solid boundaries as the WALE model [45]. All these properties come from the very nature of the new differential operator the SGS model is based on, without requiring any dynamic procedure. The SGS energy flux is modelled using a SGS turbulent heat conductivity obtained from ν_t by $\lambda_t = \overline{\rho}\, \nu_t\, c_p / Pr_t$ where $Pr_t = 0.7$ is a constant turbulent Prandtl number.

Governing equations for solid heat transfer models.

Heat transfer in solid domains is described by the energy conservation:

$$\rho_s C_s \frac{\partial T(\mathbf{x},t)}{\partial t} = -\frac{\partial q_i}{\partial x_i} \tag{2}$$

where T is the temperature, ρ_s is the density, C_s is the heat capacity and q the conduction heat flux. The heat diffusion follows Fourier's law:

$$q_i = -\lambda_s \frac{\partial T}{\partial x_i} \tag{3}$$

where λ_s is the heat conductivity of the medium. The solid solver takes into account local changes of heat capacity and conductivity with temperature.

Numerical schemes.

The parallel LES code, AVBP [46, 47], solves the full compressible Navier-Stokes equations using a two-step time-explicit Taylor-Galerkin scheme (TTG4A) for the hyperbolic terms based on a cell-vertex formulation [48], along with a second order Galerkin scheme for diffusion [49]. TTG4A provides high spectral resolution and both low numerical dissipation and dispersion, which is particularly adequate for LES [50]. Such numerics are especially designed for LES on hybrid meshes and have been extensively validated in the context of turbulent reacting flow applications [51–53]. The TTG4A scheme provides third-order accuracy in space and fourth-order accuracy in time [54]. The major drawback of this strategy arises from the explicit nature of the solver whose time step is controlled by the low acoustic CFL number (0.7 for the present computations) preventing from reducing characteristic cell size below the wall unit scale. Therefore, for aerodynamic applications, where the viscous sub-layer needs to be computed, mesh refinements force small time steps and a higher computational cost is inferred when compared to incompressible code for example. For the most refined mesh

4

M4 (Tab. 2), about 20 000 CPU hours are necessary to simulate one flow-through time on 1024 cores of the BULL Sandy Bridge machine CURIE of the TGCC. Note that despite this clear constraint, the unstructured hybrid approach enables refinement of the mesh in zones of interest by using prisms in the wall region [55].

The parallel conduction solver AVTP is based on the same data structure and thus uses a second order Galerkin diffusion scheme [49]. Time integration is done with an implicit first order forward Euler scheme. The resolution of the implicit system is done with a parallel matrix free conjugate gradient method [56].

Computational setup.

The fluid computational domain examined is sketched in Fig. 2(a) with a view of a typical mesh in Fig. 2(b). To limit the dependency of the solution on the inlet and outlet positions, the domain extends up to $0.52\ C$ upstream the blade leading edge and $1.082\ C$ downstream the vane. The spanwise size of the domain is $0.135\ C$ with periodicity enforced on each side. This simplification neglects end-wall effects but retains the three-dimensionality of the flow and greatly reduces the number of grid cells required to model the blade. The domain used for the solid during the CHT computation corresponds to the fluid one. For the fluid region, periodicity condition is also assumed in the transverse direction in order to simulate only one flow passage. These two periodicity directions are justified by the experimental setup as described in [32].

Typical unstructured meshes of complex geometries consist in tetrahedra. In order to provide the right viscous stress and heat flux at the wall, the grid cells adjacent to the wall must be inside the viscous sublayer. This condition requires a high density of very small grid cells close to the wall that leads to expensive simulations. When the boundary layer is explicitly resolved, using prismatic layers close to wall surfaces is more efficient than using tetrahedra. First, quadrilateral faces normal to the wall provide good orthogonality and grid-clustering capabilities that are well suited to thin boundary layers, whereas the triangulation in the tangential direction allows for more flexibility in surface modeling. Second, for the same spatial resolution in the normal direction, the prismatic layer approach uses less elements and leads to a higher minimum cell volume than the full tetrahedral grid approach because prismatic elements can have a larger aspect ratio. Thus, a hybrid approach with prismatic layers in the near-wall region and tetrahedra in the main duct as shown in Fig. 2(b), is adopted to: (1) reduce the number of cells in the nearby region of the wall, (2) meet the preferential directions of the boundary layer flow and (3) limit the constraint on the acoustic time step. The solution adopted has five layers of prisms where the vertical length of the prism Δy is smaller than the triangle base-length Δx or Δz (here, $\Delta x \approx \Delta z$). A limit is imposed to this mesh adaptation to avoid numerical errors in these layers: the aspect ratio of the first and thinnest layer is set to $\Delta x \approx \Delta z \approx \alpha \Delta y$, with α lower than
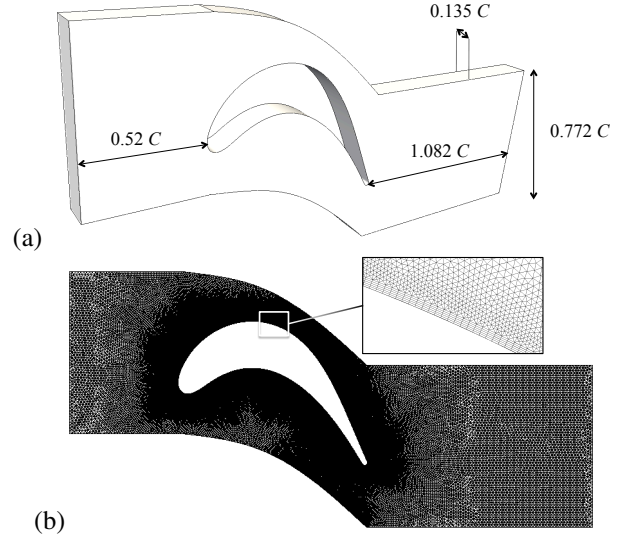

(a)

(b)

FIGURE 2. (a) SKETCH OF THE FLUID COMPUTATIONAL DOMAIN AND (b) DETAIL OF THE CORRESPONDING UNSTRUCTURED MESH GRID.

8 (i.e., $x^+ \approx z^+ \approx \alpha y^+$) in agreement with known observations and boundary layer scales [11]. Maximum cell size in the domain is fixed to 1 mm. A convergence study of the wall friction and wall heat flux depending on wall resolution Δy have been done based on four meshes. Table 2 gives the main properties of the four meshes.

The solid mesh requirements are less stringent. It is composed of 1.8 M tetrahedral cells with a characteristic size of 0.2 mm on the fluid / solid interface as well as close to the ten cooling holes and with a characteristic size of 1 mm elsewhere. The fluid and solid meshes are non-conformal at their interface where a linear interpolation is used to interpolate physical fields exchanged by the solvers during the CHT computation.

The σ subgrid model is used in conjunction with isothermal no-slip wall conditions. This model is designed to provide correct levels of turbulent viscosity down to the wall and no wall model is required. Uniform total pressure and total temperature profiles with velocity angle are imposed at the inlet of the fluid domain using the Navier-Stokes Characteristic Boundary Condition (NSCBC) formalism [57]. Static pressure is enforced at the outlet boundary in characteristic NSCBC form accounting for transverses terms [58].

FLOW AND HEAT TRANSFER ANALYSIS

In this section, the main flow features captured by the LES are first analyzed with the results obtained on mesh #4. The grid convergence from mesh #1 to #4 is then assessed based on the proper resolution of the flow characteristics around the blade. For

TABLE 2. PROPERTIES OF THE FOUR MESHES USED FOR THE FLUID.

Mesh #	M1	M2	M3	M4
Δy (mm)	0.0625	0.05	0.025	0.0125
mean y^+	5.7	4.6	2.5	1.3
$\Delta x/\Delta y = \Delta z/\Delta y$	4	4	4	8
# nodes	1.8 M	2.5 M	7.3 M	10.3 M
# cells	9.3 M	13.2 M	37.4 M	54.8 M
# prisms	0.3 M	0.5 M	2.2 M	2.2 M
# Wall boundary nodes	0.035 M	0.055 M	0.22 M	0.22 M
# Iterations per FTT	46 000	57 000	120 000	155 000

FIGURE 3. MAIN FLOW FEATURES RESPONSIBLE OF HEAT TRANSFER CHARACTERISTICS: VELOCITY FIELD (UP) AND ISO-SURFACE O FQ CRITERION (BOTTOM). THE SIMULATION IS DONE WITH MESH M4.

all the computations presented in this section, the wall temperature is kept constant and equal to 300 K. The strategy to reduce computational cost is to run the first LES on mesh M1 and use the final flow field to initialize the LES on mesh M2 and so one until mesh M4. For each case, six flow through times (FTT) are computed to converge and extract statistics for analysis. Thus, the statistics collection on mesh M4 leads to about 120 000 CPU hours on 1024 cores of the BULL Sandy Bridge machine CURIE of the TGCC.

Description of flow characteristics around the blade

Figure 3 presents an instantaneous visualization of the flow topology around the blade obtained on mesh #4. Starting from the leading edge to the trailing edge, the pressure side exhibits 3 main phenomena (A, B and C in Fig. 3). First, a massive flow separation (A) caused by the strong concave curvature of the blade profile on the pressure side starts shortly after the leading edge. Due to shear layer instabilities, the laminar flow is then transitionning to turbulence. This separation creates a large recirculation bubble fed by numerous turbulent eddies of different sizes. The flow then hits the pressure side and reattaches (B). Finally, the attached turbulent flow is accelerated until the trailing edge of the blade (C).

In the same manner, 4 main behaviors can be underlined on the suction side (D, E, F and G in Fig. 3). First the laminar flow accelerates up to the maximum camber point (D). Because of the consequent adverse pressure gradient, the flow strongly decelerates (E). This adverse pressure gradient yields a laminar separation bubble (F) with a free shear layer that experiences transition to turbulence. Subsequently, the separated turbulent flow reattaches and evolves downstream from a non-equilibrium turbulent boundar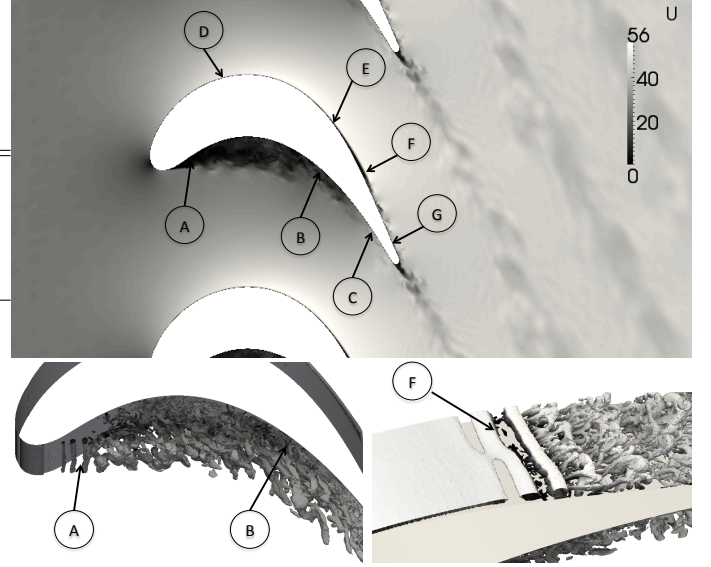y layer to an equilibrium one (G). These main flow features responsible for the heat transfer characteristics that are evidenced in the experiment are captured by all four simulations with an improved accuracy when mesh resolution increases (ie from M1 to M4).

The comparison between the mean temporal pressure distribution along the blade profile with experimental pressure measurements (Fig. 4) shows that the simulation with mesh #4 is in fair agreement with the experience. The position and intensity of the 7 main features reported previously are well predicted by the computation. On the suction side, the acceleration of the laminar boundary layer until $s/C = 0.75$ is well predicted. Then the boundary layer is exposed to an adverse pressure gradient between $s/C = 0.75$ to 1 that makes it separate. The resulting bubble is visible on the pressure plot (Fig. 4) with a plateau that starts at $s/C = 0.95$. Then when the reattachment of the transitionning boundary layer takes place, the pressure drastically increases and reaches an almost constant value until the trailing edge of the blade. The simulation tends to predict a reattachment of the boundary layer more downstream that in the experiment. On the other hand, the pressure side exhibits a strong acceleration close to the leading edge followed by a large plateau of pressure (until $s/C \approx -0.5$) that represents the large flow separation. Then the turbulent flow caused by the transition of the massive separation impacts the blade to form an attached boundary layer, causing a slight increase of pressure. From $s/C = -0.75$ to the trailing edge this turbulent boundary layer accelerates, which is evidenced by a strong reduction of the pressure.
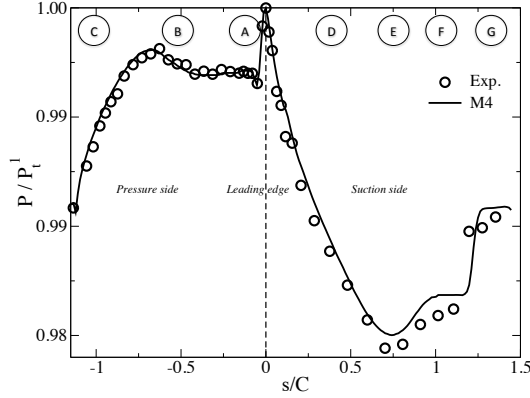
6

FIGURE 4. MEAN TEMPORAL PRESSURE DISTRIBUTION ALONG THE BLADE PROFILE. THE SIMULATION IS DONE WITH MESH M4.

Mesh convergence and heat transfer analysis

Figure 5-(a) presents the evolution of the normalized wall distance y^+ around the blade for the 4 meshes. Increasing the mesh resolution leads to a global decrease of y^+. Due to the flow topology described in the previous section and captured by the simulations done with all meshes, the shape of the four y^+ profiles are similar. This feature is directly linked to the resolution of the wall friction τ_w given for the 4 meshes in Fig. 5-(b). From the mesh convergence point of view, the wall friction levels are drastically improved from mesh #1 to mesh #3, especially in the laminar and turbulent parts of the suction side as well as in the turbulent region of the pressure side. The improvement between mesh #3 and #4 exists but is less important. Hence mesh #4 is considered to be sufficient to obtain accurate heat transfer predictions on the blade. Its maximum value of y^+ is always below 2 (Fig. 5-(a)) and the mean value around the blade is 1.3 (Tab. 2). In the other directions, the aspect ratio of the prisms that are used to mesh the boundary layer gives normalized wall distances that are kept under acceptable values [11]. Indeed, the maximum values of x^+ and z^+ are in the order of 16 (8 times the maximum of y^+, Tab. 2).

The mesh convergence is also evidenced by the heat transfer coefficient h (Fig. 6-(a)) defined by Eq. 1 with $T_{wall}(s) = 300$ K. The results from meshes #3 and #4 are almost superposed except at the leading edge as well as in the turbulent regions of both the suction and pressure sides. With the finer grid, the prediction of the HTC is very close to the experimental measurements on a large part of the blade wall. The simulation captures the influence of the flow topology on the heat transfer around the blade. To better describe the HTC profile and to give more insights on the flow behavior, Figure 6-(b) gives the evolutions of the dynamic and thermal boundary layer thicknesses along the suction side as well as the separation distance obtained with the compu-
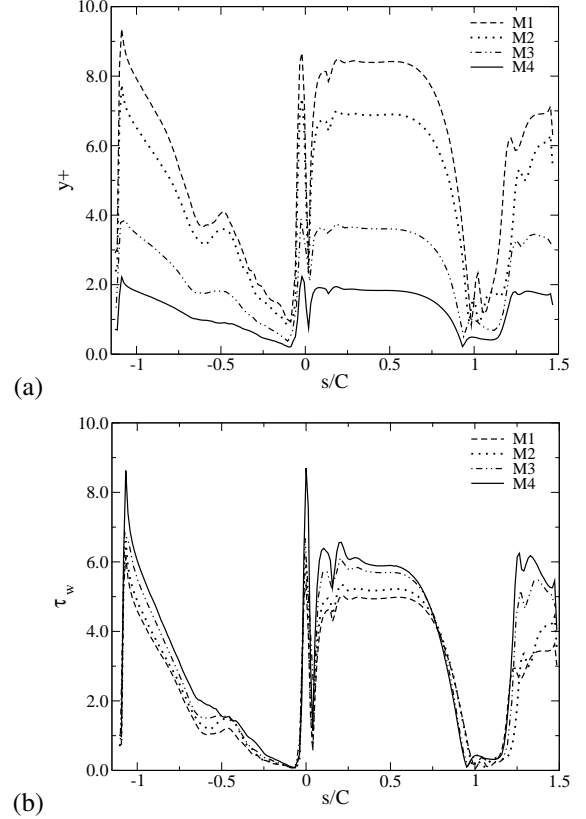

(a)

(b)

FIGURE 5. (a) Y^+ AND (b) WALL FRICTION τ_w DISTRIBUTIONS ALONG THE BLADE PROFILE FOR THE 4 MESHES.

tation done with mesh #4. The dynamic boundary layer thickness is defined as the distance across the boundary layer from the wall to a point where the flow velocity has essentially reached the local free stream velocity. This distance is defined normal to the wall, and the point where the flow velocity is essentially that of the free stream is defined as the point where the wall tangential velocity reaches 99% of its maximum on the local profile. The thermal boundary layer thickness is similarly the distance from the wall at which the temperature is 99% of the maximum temperature found on the local profile. Interestingly, the dynamic and the thermal boundary thicknesses are almost equal on a large part of the suction side, the thermal one being always thinner. Indeed, they increase in a same manner from the leading edge to a region close to the reattachment point where the dynamic thickness continues to increase while the thermal one decreases. On a first part of the suction side, the evolution of the thicknesses allows the clear identification of two accelerations zones corresponding to two different slopes of the boundary thickness (from $s/C = 0$ to 0.25 and from $s/C = 0.25$ to 0.75). At $s/C = 0.75$, the adverse pressure gradient creates another change in the slope of the thicknesses that is conserved until the beginning of the

7

flow separation (i.e. when the separation distance starts increasing): the downturn of the flow causes a thickening of the boundary layer. Because of the flow separation, the boundary layer is pushed away from the wall in the flow creating a drastic increase of the thicknesses at $s/C = 0.95$. At the end of the separation, when the size of the separation distance decreases, the dynamic thickness reaches a plateau followed by a new drastic increase when the flow reattaches and the boundary layer becomes turbulent. Note that the plateau of dynamic boundary thickness from $s/C = 1.3$ to 1.5 is a post processing artifact.

From Fig. 6-(a), the leading edge exhibits the highest convective heat exchange caused by the thin boundary layer occurring at the stagnation point. Along the suction side, the simulation first captures the rapid decrease of heat transfer due to the strong acceleration of the flow and the thickening of the laminar boundary layer (from $s/C = 0$ to 0.25). It then shows a moderate decrease of h from $s/C = 0.25$ to 0.75 linked to a slower increase of the boundary thickness, followed by a strong decrease caused by the adverse pressure gradient that suddenly thickens the boundary layer thickness from $s/C = 0.75$ to 0.95. Finally a very low level of convective heat transfer is obtained when the laminar flow separates from the wall followed by a drastic increase due to the transition of the laminar boundary layer that finished with a pic when the flow reattaches ($s/C = 1.25$). As underlined for the pressure profile, the simulation predicts a reattachment of the flow slightly downstream the experimental measurements. Along the pressure side, the simulation captures the rapid decrease of heat transfer caused by the strong acceleration of the laminar flow followed by a progressive increase in the recirculation zone. A maximum of the convective heat transfer in the reattachment region is then followed by a slight decrease of the heat transfer coefficient caused by the acceleration of the turbulent boundary layer. While the computation provides good overall levels of heat transfer coefficient, three regions of underestimation and one of overestimation can be seen. The largest underestimate is located at the leading edge where the boundary layer is known to be very thin. The heat transfer is also underestimated near the trailing edge on the suction side where the turbulent boundary layer reattaches as well as on the pressure side where the large separation takes place. This last discrepancy may be caused by under-resolved turbulent eddies that are formed in the separation bubble and participate to the heat transfer. Finally, the computation seems to overestimate heat transfer at the trailing edge. The next section on the conjugate heat transfer analysis gives some insight on this point.

In summary, with the more refined mesh (#4) the isothermal LES gives accurate predictions of the flow structure around the blade and gives insights to explain its complex behavior. The convective heat transfer coefficient is also accurately predicted by this high fidelity simulation. The next step is then the prediction of the temperature distribution in the blade that is done by a conjugate heat transfer simulation.
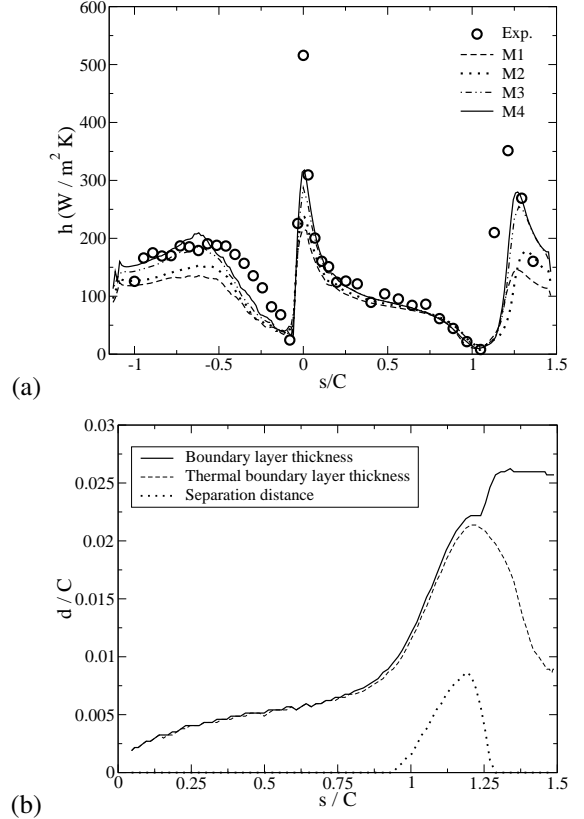

(a)

(b)

FIGURE 6. (a) CONVECTIVE HEAT TRANSFER COEFFICIENT h DISTRIBUTION ALONG THE BLADE PROFILE FOR THE 4 MESHES AND (b) EVOLUTIONS OF BOUNDARY LAYER THICKNESSES ALONG THE SUCTION SIDE OF THE BLADE.

CONJUGATE HEAT TRANSFER ANALYSIS

This section presents the CHT computation performed to predict the temperature distribution in the blade. The airfoils material is a titanium alloy for which experimentalists give a thermal conductivity of about $\lambda_s \approx 7\ \mathrm{W \cdot m^{-1} \cdot K^{-1}}$. For the coupled simulation, the conductivity follows a second order polynomial law with the temperature T fitted:

$$\lambda_s = 3.2288 + 0.0091T + 7\ 10^{-6}T^2\ (\mathrm{W \cdot m^{-1} \cdot K^{-1}}) \quad (4)$$

The density is fixed to $\rho_s = 4420\ \mathrm{kg \cdot m^{-3}}$ and the heat capacity is fitted with a second order polynomial as:

$$C_s = -80.131 + 2.8794T - 0.003085T^2\ \mathrm{J \cdot K^{-1}} \quad (5)$$

The solid blade is meshed with 1.8M tetrahedral cells (360 567 nodes). Convective conditions are imposed in the 10 cooling holes inside the blade with convective temperatures and heat

transfer coefficients provided by experimentalists. For the conjugate simulations, the wall heat fluxes computed by the fluid solver are imposed as a boundary condition to the solid part and the temperature of the solid surface is given back to the fluid wall. The target of the simulation is to obtain a converge thermal solution in the blade. To decrease the restitution time of the computation without simulating the whole transient temperature evolution of the solid temperature, the non-synchronized coupling approach proposed by [22] is used. To ensure the stability of this coupling, information at the fluid/solid interface is exchanged with a very high frequency [22, 59]. Exchanges are done every iteration of the thermal solver and after 10 iterations of the fluid one. In terms of physical time, the solid boundary conditions are updated each 20 ms while the surface temperature of the fluid is updated every 200 ns. This leads to a ratio of acceleration of the convergence of $\tau_s = 10^5 \ \tau_f$, where τ_s is the time spent in the solid and τ_f in the fluid. The coupled system reaches a quasi steady state after 2 FTT in the fluid solver corresponding to 2 characteristic times in the solid. Then, six FTT are computed to converge and extract statistics for analysis leading to a total CPU cost of about 160 000 hours on 1024 cores of the BULL Sandy Bridge machine CURIE of the TGCC.

Figure 7-(a) presents the distribution of temperature obtained at convergence of the coupled simulation around the blade. The solution is far from an isothermal wall at 300 K. The mean temperature of the profile is about $\overline{T}_{CHT} = 294.7$ K with a mean standard deviation of $\sigma_{\overline{T}_{CHT}} = 5.2$ K. The CHT results are in very good accordance with the experimental temperature profile both in terms of shape and level. The underestimations of convective heat transfer underlined previously lead to under-predictions of the temperature levels. As for the HTC, the most important under-prediction takes place at the leading edge and seems to have an influence at the beginning of the suction side, shifting the profile to lower temperatures. An other important region of temperature underestimation is the large recirculation zone on the pressure side. Finally, the temperature in the transition region of the suction side (from s/C=1 to 1.25) seems to be under-predicted as well.

The convective heat transfer coefficients from the isothermal computation ($T_{wall}(s)$=300 K) and the coupled simulation are compared to the experimental ones in Fig. 7-(b). For the coupled case, the wall temperature $T_{wall}(s)$ is taken as the local temperature obtained by the CHT computation given in Fig. 7-(a). The results from the two simulations are superimposed on a large part of the profile. The main region of difference is the trailing edge on both the suction and pressure sides where the coupled results improve the prediction of the HTC. The assumption of constant temperature at 300K to extract the convective coefficient is wrong in this region where the temperature is predicted to be higher. Having a good estimate of the temperature allows a better prediction of the correct heat flux. This trailing edge region is thus an example where Newton's law of cooling is not
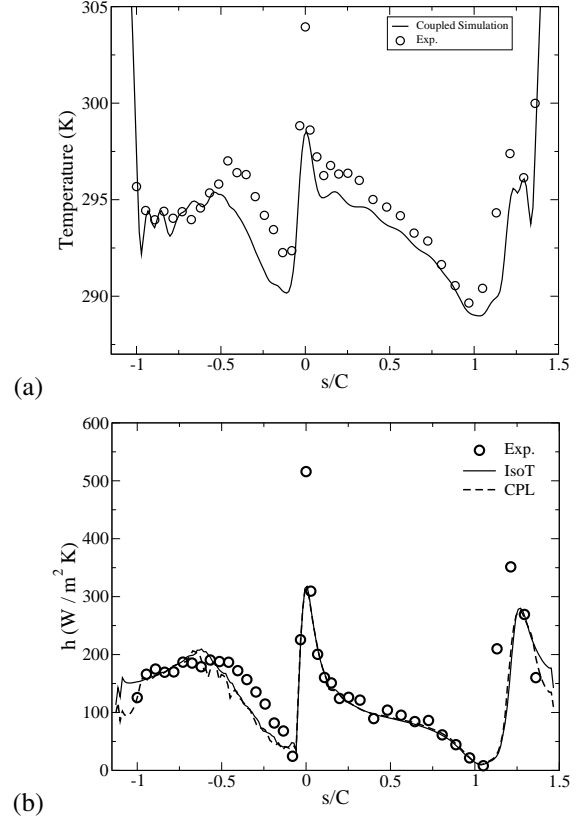

(a)

(b)

FIGURE 7. (a) TEMPERATURE DISTRIBUTION AROUND THE BLADE OBTAINED BY CHT AND (b) COMPARISON OF CONVECTIVE HEAT TRANSFER COEFFICIENT OBTAINED WITH AN ISOTHERMAL COMPUTATION (IsoT) AND THE COUPLED SIMULATION (CPL).

applicable, ie where a single heat transfer coefficient that does not vary significantly across the temperature-difference ranges covered during cooling and heating can be used.

The CHT simulation gives accurate distribution of heat transfer coefficient and temperature of the blade. It is then worth checking the dependence of the temperature distribution input parameters with uncertainty as the material conductivity and the temperature and convective coefficient in the cooling holes.

UNCERTAINTY QUANTIFICATION ON THE BLADE TEMPERATURE

The two main uncertain parameters of the solid model are the conductivity of the material as well as the convective conditions imposed in the cooling holes. To check the dependence of these two parameters on the temperature distribution inside the blade, uncertainty quantifications (UQ) are carried out. To do so, only the thermal solver is used with the boundary conditions

TABLE 3. STATISTICS OF SOLID CONDUCTIVITY OBTAIN IN THE CHT SIMULATION.

	Temperature (K)	Conductivity (W·m⁻¹·K⁻¹)
Min	287	6.42
Max	315	6.79
Mean	291	6.47

obtained by the coupled simulation on the blade wall in terms of convective temperature (T_1^t from Tab. 1) and coefficient ($h(s)$ from Fig. 7-(b)).

As exposed before, the convective heat transfer coefficient can be considered independent of the operating temperature difference between the solid and the flow in a wide part of the blade. Moreover, the range of blade temperature obtained at the most critical part (ie the trailing edge) during the UQ study is rather small. Thus, it is consistent to use a fixed profile of $h(s)$ for this study without recomputing the whole CHT simulation for all the UQ investigations.

The selected UQ method is therefore a non-intrusive method around the AVTP solver based on the stochastic collocation at Clenshaw-Curtis quadrature points with the same weights for each parameter. To obtain the desired statistics, the output temperature function is built from the sampling using Lagrange polynomials [60–63]. The convergence of temperature mean and standard deviation is fast and obtained with only 3 Clenshaw-Curtis quadrature points.

Uncertainty quantification on thermal conductivity

Experimentalists approximate the conductivity by $\lambda_s \approx 7$ W·m⁻¹·K⁻¹. Table 3 gives the minimum, maximum and mean values of the conductivity obtained by the coupled computation with a conductivity that depends on temperature (Eq. 4). The conductivity given by experimentalists is close to the one obtained in the CHT computation but remains outside the range of variation observed in the simulation. As the temperature distribution in the blade is directly linked to the equilibrium between solid and fluid conductivities, uncertainty quantification of the blade temperature distribution to the solid conductivity is of primary interest. Two mean values of the solid conductivity are tested ($\bar{\lambda}_s^7 = 7$ W·m⁻¹·K⁻¹ and $\bar{\lambda}_s^{6.5} = 6.5$ W·m⁻¹·K⁻¹) with an uncertainty of 10%. For this study, the conductivity is thus taken independent of the temperature.

Figure 8 presents the mean and 95% confidence interval of the temperature distribution obtained around the blade from the above uncertain inputs. The temperature profile is not really modified by such a small uncertainty on conductivities. The standard deviation of the temperature ranges from 0.035 K near the separation region on the suction side for the case with $\bar{\lambda}_s^7$ (0.025 K for $\bar{\lambda}_s^{6.5}$) to 0.88 K (resp. 0.6 K for $\bar{\lambda}_s^{6.5}$) close to the trailing
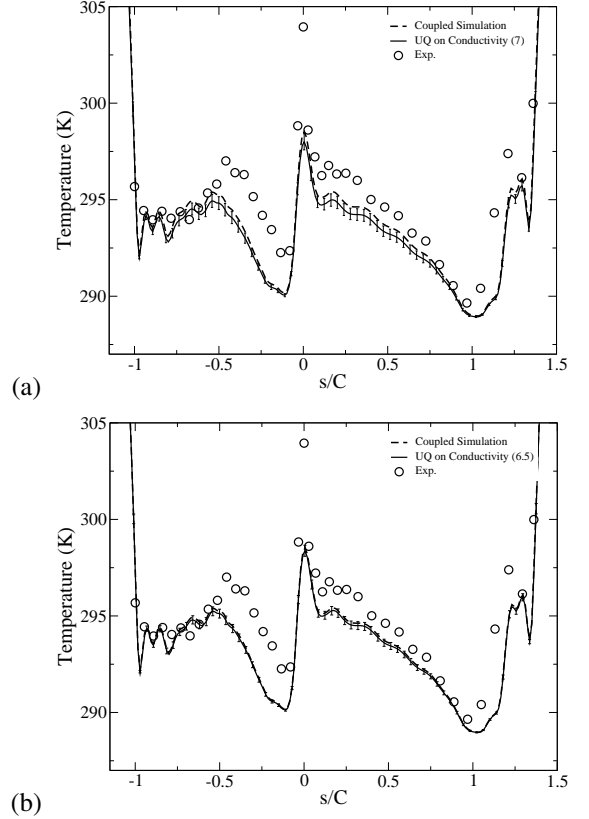

(a)

(b)

FIGURE 8. MEAN AND 95% CONFIDENT INTERVAL OF THE TEMPERATURE DISTRIBUTION AROUND THE BLADE WITH RESPECT TO UNCERTAINTY IN CONDUCTIVITY WITH A MEAN VALUES OF (a) $\bar{\lambda}_s = 7$ W·m⁻¹·K⁻¹ and (b) $\bar{\lambda}_s = 6.5$ W·m⁻¹·K⁻¹.

edge. Peak values are observed at the leading edge as well as in the turbulent region of the boundary layers both in the suction and pressure sides. The average values of the temperature standard deviations are about 0.26 K for $\bar{\lambda}_s^7$ and 0.18 K for for $\bar{\lambda}_s^{6.5}$, which represent less than 0.1% of the mean temperature $\bar{T}_{CHT}$ and less than 5% of the dispersion of the temperature profile $\sigma_{\bar{T}_{CHT}}$ (respectively 294.7 K and 5.2 K).

Finally, the temperature distribution obtained by the coupled simulation is outside the 95% confidence interval of the case $\bar{\lambda}_s^7$ whereas it belongs to the case $\bar{\lambda}_s^{6.5}$. It is interesting to underline that none of the computations done with the different values of the conductivity that are independent of the temperature (a total of 10 for this UQ study) are able to reproduce the profile obtained with the temperature dependency.

The results of this first UQ study show that the level of uncertainty on the conductivity is not significant to affect the wall temperature predictions done with the CHT computation.

10

Uncertainty quantification on the cooling temperatures

Experimentalists have measured the mass flow of each cooling channel as well as the temperatures at inlet and outlet. The cooling temperatures have been determined as the average of inlet and outlet temperatures of the coolant, assuming that the heat flux into the coolant is symmetric to midspan of the blade. Furthermore, the difference between inlet and outlet temperatures is very small. The maximum temperature difference measured of the 10 holes is 2.5 K with an average difference of approximately 1 K. The heat transfer coefficients are then calculated with a correlation for turbulent flow in pipes [64]. For each holes, a couple of cooling temperature and convective coefficient are thus provided. Of course the uncertainty in this case can come from the estimation of the convective coefficient as well as from the cooling temperatures. As both are linked, the choice has been made to concentrate on the cooling temperature. The experimental uncertainty on the cooling temperature is about 0.85%. Then, as there are 10 holes, it is possible to define a UQ framework with 10 parameters being the convective coefficient of each hole, each associated with independent uncertainty. Nevertheless, resolving such a large problem with a collocation method is prohibitively expensive on a full tensor grid, and probably not so interesting for the case studied here. Indeed, because of the measurement technique, the uncertainties on the different hole temperatures are linked. Consequently, the analysis is divided into two parts: the first one investigates the role of separated holes in the uncertainty quantification process. The second one considers a global error that affects all the 10 holes in the same way.

Figure 9 presents the mean and 95% confidence interval of the temperature distribution around the blade resulting from the UQ done on cooling temperatures for holes number #1 and #4. The uncertainty on a hole has a local effect on the temperature distribution that is not negligible. The standard deviation of temperature ranges from 0 K far away from the uncertain hole to 1.25 K close to it when hole #1 is considered and 0.9 K for hole # 4 (Figure 10-a). These uncertainties represent about 0.4% of the mean temperature $\overline{T}_{CHT}$ and 24% of the dispersion of the temperature profile $\sigma_{\overline{T}_{CHT}}$ for hole #1 and 0.3% and 17% for hole #4 respectively.

It is suspected that the uncertainty effects of two nearby holes can combine to give a high level of output uncertainties on the blade temperature. Uncertainty quantification of the blade temperature distribution to the temperature inside all the cooling holes at the same time is reported now. The combination effect is clearly evidenced on Fig. 10-(a) both on the pressure and suction sides. On the one hand, the uncertainties on the leading-edge and trailing-edge temperatures are mainly controlled by hole #1 and hole #10, respectively. On the other hand uncertainties obtained by the UQ involving the 10 holes at the same time are more important than the ones obtained by considering hole by hole. Figure 10-(b) presents the mean and 95% confidence interval of the temperature distribution around the blade resulting
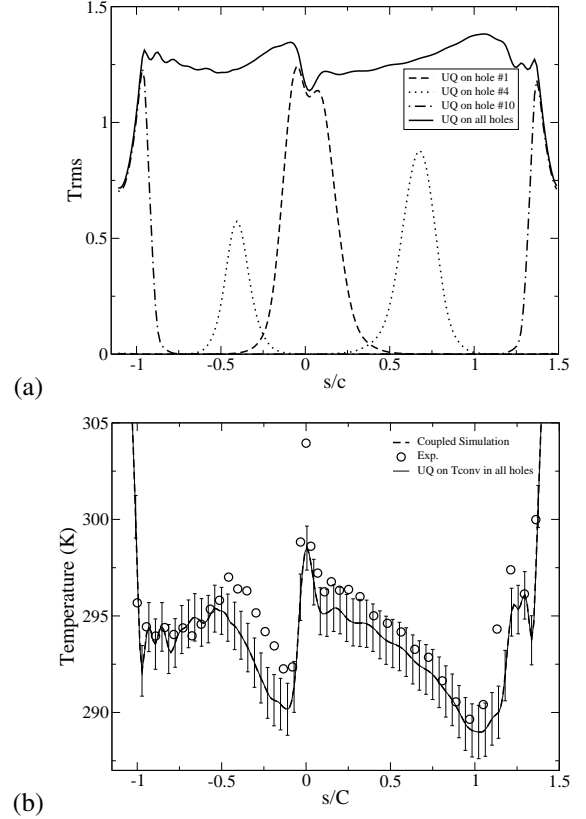

(a)

(b)

FIGURE 10. RMS TEMPERATURE PROFILES AROUND THE BLADE OBTAINED BY UQ SIMULATIONS DONE ON SEPARATED CONVECTIVE TEMPERATURE IN HOLES COMPARED TO THE FULL UQ IN ALL HOLES (a) AND MEAN AND 95% CONFIDENT INTERVAL OF THE TEMPERATURE DISTRIBUTION AROUND THE BLADE WITH RESPECT TO UNCERTAINTY IN CONVECTIVE CONDITIONS IN ALL THE HOLES (b).

from this global uncertainty quantification. The temperature profile is largely affected by the knowledge of the cooling temperature: the standard deviation of the temperature ranges from 0.7 K near the trailing edge to 1.5K close the leading edge as well as in the separation zone on the suction side. The average value of the uncertainty is about 1.23 K representing almost 0.4% of the mean temperature $\overline{T}_{CHT}$ and 24% of the deviation $\sigma_{\overline{T}_{CHT}}$. Hence, the experimental measurements are included in the simulation error bars in most parts of the profile except at the leading edge and in the recirculation zone on the pressure side. This result illustrates that the flow and heat transfer are well captured on most of the blade except in these two regions.
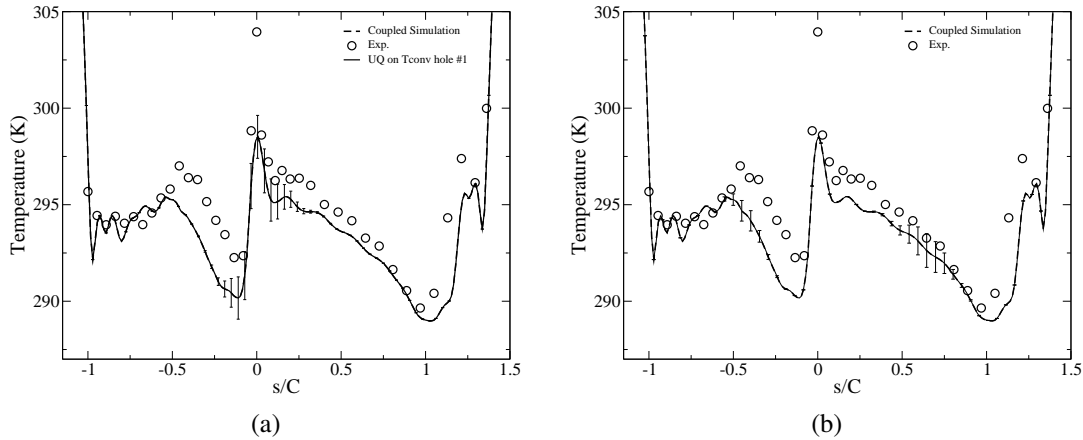
11

FIGURE 9. SPATIAL DISTRIBUTION OF RMS TEMPERATURE IN THE BLADE WITH RESPECT TO UNCERTAINTY IN CONVECTIVE CONDITIONS IN (TOP a) HOLE #1, (TOP b) HOLE #4 AND MEAN AND 95% CONFIDENT INTERVAL OF THE TEMPERATURE DISTRIBUTION AROUND THE BLADE WITH RESPECT TO UNCERTAINTY IN CONVECTIVE CONDITIONS IN (BOTTOM a) HOLE #1, (BOTTOM b) HOLE #4.

CONCLUSION

Large Eddy Simulation has been coupled with a thermal solver in order to investigate the flow field and heat transfer around a highly loaded low pressure water-cooled turbine vane at moderate Reynolds number (150 000). The meshing strategy (hybrid grid with 5 layers of prisms at the wall and tetrahedra elsewhere) combined with a high fidelity LES solver gives accurate predictions of the wall heat transfer coefficient for isothermal computations. Mesh convergence underlines the known result that wall-resolved LES requires discretisations for which y^+ is of the order of one. The analysis of the flow field gives a comprehensive view of the main flow features responsible of heat transfer, mainly the separation bubble on the suction side that triggers transition to a turbulent boundary layer and the massive separation region on the pressure side. Underestimations of heat fluxes are observed at some critical location as the leading edge of the blade as well as the massive separation on the pressure side. While, these under-predictions lead to underestimates of the blade temperatures by the coupled process, CHT results are in a very good accordance with temperature measurements. It was shown that the heat flux obtained by the isothermal computation and by the coupled one are very similar all along the blade except at the trailing edge where CHT results are in closer agreement with experiments. In this region, Newton's law of cooling is not yet applicable and the CHT results allow to better capture the heat fluxes in this region. Finally, an uncertainty quantification showed that most of the temperature discrepancies could be explained by the cooling temperature uncertainty except at the leading edge, in the turbulent region on the suction side and in the recirculation zone on the pressure side.

REFERENCES

[1] Lakshminarayana, B., 1996. *Fluid Dynamics and Heat Transfer of Turbomachinery*. Wiley.

[2] Lefebvre, A. H., 1999. *Gas Turbines Combustion*. Taylor & Francis.

[3] Schiele, R., and Wittig, S., 2000. "Gas turbine heat transfer: Past and future challenges". *J. Prop. Power,* **16**(4), July, pp. 583–589.

[4] Dunn, M., 2001. "Convective heat transfer and aerodynamics in axial flow turbines". *J. Turbomach.,* **123**, pp. 637–686.

[5] Bunker, R. S., 2006. "Gas turbine heat transfer: 10 remaning hot gas path challanges". In Procceedings of GT2006. ASME Turbo Expo 2006.

[6] Tennekes, H., and Lumley, J. L., 1972. *A first course in turbulence*. M.I.T. Press, Cambridge.

[7] Lumley, J. L., 1978. "Computational modeling of turbulent flows". *Adv. Appl. Mech.,* **18**, pp. 123–176.

[8] Pope, S. B., 2000. *Turbulent flows*. Cambridge University Press.

[9] Wilcox, D., 1988. "Reassessment of the scale-determining equation for advanced turbulence models". *AIAA Journal,*

26, pp. 1299–1310.

[10] Hirsch, C., 1990. *Numerical Computation of Internal and External Flows*, Vol. 2. John Wiley & Sons, New York.

[11] Sagaut, P., 2000. *Large Eddy Simulation for incompressible flows*. Scientific computation series. Springer-Verlag.

[12] Abu-Ghannam, B., and Shaw, R., 1980. "Natural transition of boundary layers - the effects of turbulence, pressure gradient, and flow history.". *J. of Mechanical Engineering Science, 22*(5), pp. 213–228.

[13] Mayle, R. E., 1991. "The role of laminar-turbulent transition in gas turbine engines". *J. Turbomach., 113*, October, pp. 509–537.

[14] Johnson, M. W., 1994. "A bypass transition model for boundary layers.". *J. Turbomachinery, 116*(4), pp. 759–764.

[15] Smirnov, E., and Smirnovsky, A., 2009. "Turbine vane cascade heat transfer predictions using a modified version of the Re_{θ_t} laminar-turbulent transition model.". *Int. Symp. On Heat Transfer in Gas Turbine Systems*.

[16] Wlassow, F., Duchaine, F., Leroy, G., and Gourdain, N., 2010. "3d simulation of coupled fluid flow and solid heat conduction for the calculation of blade wall temperature in a turbine stage.". In ASME Turbo expo, GT2010-22513, ed.

[17] Lutum, E., and Cottier, F., 2011. "Aerothermal predictions on a highly loaded turbine blade including effects of flow separation". In 9th European Turbomachinery Conference.

[18] Rozati, A., 2007. "Large eddy simulation of leading edge film cooling: Flow physics, heat transfer, and syngas ash deposition". PhD thesis, Virginia Polytechnic Institute and State University.

[19] Boudier, G., Gicquel, L. Y. M., Poinsot, T., Bissières, D., and Bérat, C., 2007. "Comparison of LES, RANS and experiments in an aeronautical gas turbine combustion chamber". *Proc. Combust. Inst., 31*, pp. 3075–3082.

[20] Sagaut, P., and Deck, S., 2009. "Large-eddy simulation for aeronadymics: status and perspectives". *Phil. Trans. R. Soc. Lond., 367*, pp. 2849–2860.

[21] Leonard, T., Duchaine, F., Gourdain, N., and Gicquel, L., 2010. "Steady / unsteady reynolds averaged navier-stokes and large eddy simulastions of a turbine blade at high subsonic outlet mach number". In ASME Turbo Expo, GT2010-22469, ed.

[22] Duchaine, F., Corpron, A., Pons, L., Moureau, V., Nicoud, F., and Poinsot, T., 2009. "Development and assessment of a coupled strategy for conjugate heat transfer with large eddy simulation: Application to a cooled turbine blade". *Int. J. Heat Fluid Flow, 30*(6), pp. 1129–1141.

[23] Bhaskaran., R., and Lele, S., 2010. "Large eddy simulation of free-stream turbulence effects on heat transfer to a high-pressure turbine cascade". *J. Turb., 11*(6), pp. 1–15.

[24] Maheu, N., Moureau, V., and Domingo, P., 2012. "High fidelity simulation of heat transfer between a turbulent flow and a wall". In ERCOFTAC ETMM9.

[25] Collado, E., Gourdain, N., Duchaine, F., and Gicquel, L., 2012. "Effects of free-stream turbulence on high pressure turbine blade heat transfer predicted by structured and unstructured LES". *Journal of Heat and Mass Transfer, 55*(21-22), pp. 5754– 5768.

[26] Heselhaus, A., and Vogel, D. T., 1995. "Numerical simulation of turbine blade cooling with respect to blade heat conduction and inlet temperature profiles". In ASME, SAE, and ASEE, Joint Propulsion Conference and Exhibit, 31st, no. AIAA-1995-3041.

[27] Sondak, D. L., and Dorney, D. J., 2000. "Simulation of coupled unsteady flow and heat conduction in turbine stage". *J. Prop. Power, 16*(6), pp. 1141–1148.

[28] Papanicolaou, E., Giebert, D., Koch, R., and Schultz, A., 2001. "A conservation-based discretization approach for conjugate heat transfer calculations in hot-gas ducting turbomachinery components". *Int. J. Heat and Mass Transfer, 44*, pp. 3413–3429.

[29] Garg, V., 2002. "Heat transfer research on gas turbine airfoils at NASA GRC". *Int. J. Heat Fluid Flow, 23*(2), April, pp. 109–136.

[30] Bohn, D., Ren, J., and Kusterer, K., 2005. "Systematic investigation on conjugate heat transfer rates of film cooling configurations". *Int. J. Rotating Machinery , 2005*(3), pp. 211–220.

[31] Alonso, J. J., Hahn, S., Ham, F., Herrmann, M., Iaccarino, G., Kalitzin, G., LeGresley, P., Mattsson, K., Medic, G., Moin, P., Pitsch, H., Schlüter, J., Svard, M., der Weide, E., You, D., and Wu, X., 2006. "Chimps: a high-performance scalable module for multi-physics simulation". In 42nd AIAA/ASME/SAE/ASEE Joint Propulsion Conference & Exhibit, no. AIAA-Paper 2006-5274.

[32] Ladisch, H., Schulz, A., and Bauer, H.-J., 2009. "Heat transfer measurements on a turbine airfoil with pressure side separation". In ASME Turbo Expo 2009 : Power for Land, Sea, and Air.

[33] Turner, A., 1970. Heat transfer instrumentation. Tech. Rep. AGARD-CP-73, AGARD.

[34] Wittig, S., Schulz, A., and Bauer., H., 1985. Effects of wakes on the heat transfer in gas turbine cascades. Tech. Rep. AGARD-CP-390, AGARD.

[35] Schultz, M. S. A., and Wittig, S., 2005. "Surface roughness effects on external heat transfer on a hp turbine vane". *ASME-Paper GT2004-53114, 127*, pp. 200–208.

[36] Cadieux, F., Domaradzki, J., Sayadi, T., Bose, S., and Duchaine, F., 2012. "Dns and les of separated flows at moderate reynolds numbers". In Bulletin of the American Physical Society, Vol. 57.

[37] Buis, S., Piacentini, A., and Déclat, D., 2005. "PALM: A Computational Framework for assembling High Perfor-

mance Computing Applications". *Concurrency and Computation, 18*(2), pp. 231–245.

[38] Piacentini, A., Morel, T., Thevenin, A., and Duchaine, F., 2011. "Open-palm: an open source dynamic parallel coupler.". In In IV International Conference on Computational Methods for Coupled Problems in Science and Engineering.

[39] Poinsot, T., and Veynante, D., 2005. *Theoretical and Numerical Combustion*. R.T. Edwards, 2nd edition.

[40] Ferziger, J. H., and Perić, M., 1997. *Computational Methods for Fluid Dynamics*. Springer Verlag, Berlin, Heidelberg, New York.

[41] Smagorinsky, J., 1963. "General circulation experiments with the primitive equations: 1. the basic experiment.". *Mon. Weather Rev., 91*, pp. 99–164.

[42] Chassaing, P., 2000. *Turbulence en mécanique des fluides, analyse du phénomène en vue de sa modélisation à l'usage de l'ingénieur*. Cépaduès-éditions, Toulouse, France.

[43] Baya Toda, H., Cabrit, O., Balarac, G., Bose, S. T., Lee, J., Choi, H., and Nicoud, F., 2010. "A subgrid-scale model based on singular values for LES in complex geometries". In *Proc. of the Summer Program*. Center for Turbulence Research, NASA Ames/Stanford Univ., pp. 193–202.

[44] Nicoud, F., H, B. T., Cabrit, O., S., B., and Lee, J., 2011. "Using singular values to build a subgrid-scale model for large eddy simulations". *Phys. Fluids, 23*(8), Aug.

[45] Nicoud, F., and Ducros, F., 1999. "Subgrid-scale stress modelling based on the square of the velocity gradient". *Flow, Turb. and Combustion, 62*(3), pp. 183–200.

[46] Schønfeld, T., and Rudgyard, M., 1999. "Steady and unsteady flows simulations using the hybrid flow solver avbp". *AIAA Journal, 37*(11), pp. 1378–1385.

[47] Mendez, S., and Nicoud, F., 2008. "Large-eddy simulation of a bi-periodic turbulent flow with effusion". *J. Fluid Mech., 598*, pp. 27–65.

[48] Selmin, V., 1987. Third-order finite element schemes for the solution of hyperbolic problems. Tech. Rep. 707, INRIA report.

[49] Donea, J., and Huerta, A., 2003. *Finite Element Methods for Flow Problems*. John Wiley & Sons Inc, New York.

[50] Lamarque, N., 2007. "Schémas numériques et conditions limites pour la simulation aux grandes échelles de la combustion diphasique dans les foyers d'hélicoptère". Phd thesis, INP Toulouse.

[51] Boileau, M., Staffelbach, G., Cuenot, B., Poinsot, T., and Bérat, C., 2008. "LES of an ignition sequence in a gas turbine engine". *Combust. Flame, 154*(1-2), pp. 2–22.

[52] Staffelbach, G., Gicquel, L., Boudier, G., and Poinsot, T., 2009. "Large eddy simulation of self-excited azimuthal modes in annular combustors". *Proc. Combust. Inst., 32*, pp. 2909–2916.

[53] Gicquel, L., Staffelbach, G., and Poinsot, T., 2012. "Large

eddy simulations of gaseous flames in gas turbine combustion chambers". *Progress in Energy and Combustion Science, 38*(6), pp. 782–817.

[54] Colin, O., and Rudgyard, M., 2000. "Development of high-order taylor-galerkin schemes for unsteady calculations". *J. Comput. Phys., 162*(2), pp. 338–371.

[55] Boileau, M., Duchaine, F., Jouhaud, J.-C., and Sommerer, Y., 2013. "Large eddy simulation of heat transfer around a square cylinder using unstructured grids". *AIAA Journal, doi:10.2514/1.J051800*.

[56] Frayssé, V., Giraud, L., Gratton, S., and Langou, J., 2005. "A set of GMRES routines for real and complex arithmetics on high performance computers". *ACM Trans. Math. Softw., 31*(2), pp. 228–238.

[57] Poinsot, T., Echekki, T., and Mungal, M. G., 1992. "A study of the laminar flame tip and implications for premixed turbulent combustion". *Combust. Sci. Tech., 81*(1-3), pp. 45–73.

[58] Granet, V., Vermorel, O., Leonard, T., Gicquel, L., , and Poinsot, T., 2010. "Comparison of nonreflecting outlet boundary conditions for compressible solvers on unstructured grids". *AIAA Journal, 48*(10), pp. 2348–2364.

[59] Giles, M., 1997. "Stability analysis of numerical interface conditions in fluid-structure thermal analysis". *Int. J. Numer. Meth. Fluids, 25*(4), pp. 421–436.

[60] Xiu, D., and Hesthaven., J., 2005. "High-order collocation methods for differential equations with random inputs". *SIAM J. Sci. Comput., 27*(3), pp. 1118–1139.

[61] Loeven, G., Witteveen, J., and Bijl, H., 2007. "Probabilistic collocation: an efficient nonintrusive approach for arbitrarily distributed parametric uncertainties". In 45th AIAA Aerospace Sciences Meeting, no. AIAA-2007-317.

[62] Pecnik, R., Witteveen, J., and Iaccarino, G., 2011. "Uncertainty quantification for laminar-turbulent transition prediction in rans turbomachinery applications". In 49th AIAA Aerospace Sciences Meeting, no. AIAA-2011-0660.

[63] Christophe, J., Sanjosé, M., and Moreau, S., 2012. "Uncertainty quantification of a low-speed axial fan self-noise". In Proceedings ISROMAC Conference 2012.

[64] Gnielinski, V., 1975. "Neue gleichungen für den wärme- und den stoffübergang in turbulent durchströmten rohren und kanälen". *Forschung im Ingenieurwesen, 41*, pp. 8–16.